RSC Advances

ROYAL SOCIETY OF CHEMISTRY

www.rsc.org/advances

RSC Advances

ARTICLE

Enhanced visible-light-induced photocatalytic activity of anatase TiO_2 nanocrystallite derived from CMK-3 and tetrakis (dimethylamino) titanium†

Xiaoyin Zhang, [a,b] Ye Zhang, [*a] Dawei Liu, [a,b] Junpeng Feng, [a,b] Ligong Zhou, [a] Ying Yang, [a] Xiangyun Guo, [a] Xuekuan Li[a]

Received 00th January 20xx,
Accepted 00th January 20xx

DOI: 10.1039/x0xx00000x

www.rsc.org/

Titanium dioxide is a typical photocatalyst in terms of green chemistry and extending the excitation light to visible light range has attracted great attention. In this work, we successfully synthesized TiO_2 nanocrystallite enriched in oxygen vacancies and traces of N-dopants by nanocasting method from functionalized mesoporous carbon sieves CMK-3 and tetrakis (dimethylamino) titanium (TDMAT), in which the functionalized CMK-3 acted as both reactant and hard-template. The obtained TiO_2-600 was well characterized by means of XRD, BET, Raman scattering, XPS, HRTEM, and EPR. Results demonstrated that TiO_2 nanoparticles possessed uniform particle size (5.0 nm), anatase phase and large surface areas (228 m^2/g) due to the space-confine effect of mesopores in CMK-3. Rhodamine B (RhB) was used as a representative organic pollutant to evaluate the photocatalytic activity under visible light irradiation. Results showed that the as-prepared TiO_2-600 performed enhanced photocatalytic activity compared to commercial P25 and the degradation rate was calculated 4.8 times higher than that of P25 under visible light irradiation. The increased photocatalytic activity of the TiO_2 catalyst can be attributed to the synergistic effect between oxygen vacancies and N-dopants.

Introduction

Nowadays, titanium dioxide TiO_2 gains its popularity in water splitting, solar cells and decomposition of pollutants as a photocatalyst, due to its environmentally friendliness, non-toxicity and low-cost[1-4]. In general, titania exists in three naturally occurring polymorphs: anatase, rutile and brookite [5] and among which anatase has been proved displaying a higher photocatalytic efficiency than other phases because of the more open structure[6].

Researchers[7-13] have shown that the surface area and crystalline size of anatase play an important role on improving the catalytic efficiency. Downsizing TiO_2 particle size to nanoscale [7, 14, 15] can not only generate reactive oxygen species[16], but improve the electron transportation rate through decreasing the transport pathway of the photogenerated charge carriers to the surface reaction sites[9]. For example, Micah. J[13] prepared anatase TiO_2 with increased crystallinity and surface areas via a continuous aqueous process and it performed higher electric capacity at low rate. M. Amin[16] synthesized TiO_2 nanoparticles and has proved the anatase particles showed superior photocatalytic activity when irradiated with UV light.

Unfortunately, the relatively wide band gap of 3.2 eV for pristine anatase TiO_2, limits its absorption located in the ultraviolet region, which need artificial ultraviolet for light excitation[9]. Sunlight is a kind of cheap and accessible light source. Therefore, much work[17, 18] has been done to extend the absorption of TiO_2 into the region of visible-light of spectrum. Introduction of oxygen vacancy into the framework of TiO_2 is one of the approaches to increase the photocatalytic activity, in which oxygen vacancy can be used as charge carrier trapping sites for inhibiting the recombination of photo-induced electro/hole pairs[15, 16, 19-21] and providing midgap band just below the conductive band [14]. What's more, DFT-based studies [22]have demonstrated the oxygen vacancy can promote the O_2 adsorption on an initially inert stoichiometric TiO_2 (001) facet either in the superoxide state(O_2^{1-}) or the peroxide state(O_2^{2-}). On the other hand, N doping has been also proved facilitating to narrow the band gap and extend the absorption spectra into visible areas[18, 23, 24]. The introduced N element can affect the electronic coupling effect by incorporating with TiO_2 matrix and introduce some impurity energy level just above the valence band or below the conduction band of TiO_2, the as-produced impurity energy level from dopants can help to extend the visible absorption[9] by accelerating electron transport rate or prolonging lifetime of photogenerated hole–electron pairs.

Hard templating (nanocasting) method is generally considered to be predictable and controllable in crystal size, morphology and structure with high suface area[25-27]. The mesoporous silica molecular sieve series (SBA-15, KIT-6, MCM-48, et al) and mesoporous carbon (CMK-3, CMK-1) are widely used as hard template because of the presence of disordered micropores between the mesopores, which ensures the replicas can be connected by bridges so as to form mesopores. The hard templates have to be removed during the nanocasting period. Mesoporous silica template is usually removed using an aqueous NaOH or HF

[a] Institute of Coal Chemistry, Chinese Academy of Sciences, Taiyuan 030001, PR China. E-mail: yzhang@sxicc.ac.cn; xyzhang428@163.com
[b] University of Chinese Academy of Sciences, Beijing 100049, PR China.
Electronic Supplementary Information (ESI) available: See DOI: 10.1039/x0xx00000x

solution, which may easily destroy the structure of some target material especially for amphoteric oxide such as TiO_2, ZnO, et al, though researchers have synthesized amphoteric oxide from SBA-15 and KIT-6 through shortening the corrosion time[26, 28], the stability of obtained materials is not optimistic. Thus mesoporous carbon has been an promising candidate with appropriate pore diameter, more importantly, it could be easily eliminated by calcination without introducing HF or NaOH solution into the system[29].

In the present paper, we synthesized TiO_2 nanocrystallite with oxygen vacancies within the mesopores of CMK-3 via the combination of organometallic chemistry and materials chemistry. Tetrakis (dimethylamino) titanium (TDMAT) was firstly used as titanium source. At the same time, functionalized CMK-3 was used as reactants as well as hard template during the synthesis of TiO_2. The structure of the obtained material was characterized in detail. The photocatalytic properties was investigated by degradation of Rhodamine B. In comparison, commercial Degussa P25 was also studied for comparison.

2 Experimental

2.1 Materials

$EO_{20}PO_{70}EO_{20}$ (M_W= 5800, Pluronic P123), hydrochloric acid (37 wt.%), sucrose(≥99.9%), concentrated sulfuric acid(98 wt.%), hydrofluoric acid (40 wt.%), TDMAT (99.9%) and toluene (99.9%) were purchased from Sigma-Aldrich. Tetraethoxysilane (TEOS) was purchased from Acros, deionized water was used throughout the experiments. All the reagents in our study are analytically pure and were used without further purification.

2.2 Synthesis procedure

2.2.1 Synthesis of SBA-15:

SBA-15 was synthesized according to the literature elsewhere[30]. The related synthesis procedure and small-angle X-ray diffraction pattern were shown in ESI (Fig. S1†).

2.2.2 Synthesis of CMK-3:

CMK-3 was prepared from SBA-15 according to the reference[31] and the as-prepared CMK-3 has typical hexagonal mesopores (Fig. S2†). Typically, 6.25 g of sucrose and 0.7 g of concentrated sulfuric acid were dispersed in 25 g of deionized water in order to obtain homogeneous solution, and then 5 g of SBA-15 was added to the above solution with vigorously stirring. The mixture was heated at 100 ℃ for 6 hours, then the temperature was increased to 150 ℃ for another 4 hours. The resulting black materials was milled into powders and repeated the above carbonation procedure with another solution (4 g of sucrose, 0.47 g of concentrated sulfuric acid and 25 g of deionized water). The obtained materials were then heated at a rate of 2 ℃·min^{-1} in argon atmosphere to reach the final temperature of 900 ℃for 2 hours. Then the composite was mixed with hydrofluoric acid (40 wt.%) for 2 days to remove the silica template. Thus obtained CMK-3 was pretreated by nitric acid solution (2 M) to modify the less functional surface.

2.2.3 Synthesis of crystalline TiO_2.

The crystalline TiO_2 was synthesized by the hard-template method, in which tetrakis (dimethylamino) titanium (TDMAT) was used as the titanium source and mesoporous carbon CMK-3 as the template. Before being used as hard-template, 2 g of CMK-3 was functionalized using 15 mL of nitric acid solution (2 M) under vigorous stirring for 2 h, donated as F-CMK-3. F-CMK-3 was dried overnight in vacuum at 150 ℃ and then kept in the airless environment. The following procedure would be carried out in glove box or on vacuum line. TDMAT dispersed in toluene was mixed with the functionalized carbon homogeneously in a Shlenk and then fluxed at 110 ℃ for 3 days under sealed conditions. The product was filtrated and washed by toluene on the vacuum line. The initial mole ratio is 37.2 C: 1 Ti: 36.5 toluene. Then the sample was exposed to air at room temperature for 1 day to promote the reaction of the residue active Ti-N bond. Finally, the composite of TiO_2 and carbon was thermal treated in argon at 600 ℃ for 5 hours following by calcination in air at 600 ℃ for another 5 hours with a ramping rate of 2 ℃/min to remove the carbon template. The obtained specimen was named as TiO_2-600.

2.3 Sample characterization

X-ray diffraction (XRD) detection was carried out on a D8 Advance X-ray powder diffractometer equipped with Cu Kα radiation (λ=1.54187 Å) at 40 kV and 40 mA. Thermogravimetric analysis (TGA) was conducted on a thermogravimetric analyzer of Setsys Evolution TGA 16/18 in air atmosphere from ambient temperature to 800 ℃ with a ramping rate of 10 ℃/min (Fig. S3†). The microstructure was examined with high-resolution transmission electron microscopy (HRTEM; JEOL-2010) at an acceleration voltage of 200 kV. X-ray photoelectron spectroscopy (XPS) was performed under an ultrahigh vacuum on a Kratos AXIS ULTRA DLD spectrometer with Al Kα radiation and a multichannel detector, the binding energies were referenced to the C 1s at 284.6 eV. Raman spectroscopy was performed using a Raman Microprobe (HR-800 Jobin-Yvon) with a 532 nm Nd:YAG excitation source at room temperature. The Brunauer–Emmett–Teller (BET) specific surface areas of the samples were determined by nitrogen adsorption–desorption isotherm measurements at 77 K on Tristar 3020. EPR spectra were recorded at room temperature with a standard Bruker EPR spectrometer, EMXPLUS10/12 (X-band, sensitivity of about 1.5 × 109 spin/G, modulation frequency = 100 kHz, microwave

frequency is 98.635 GHz). The g value is calculated by the formula $h\nu=g\beta H$ ($\beta=9.2710\times10^{-21}$ erg/G, $h=6.62620\times10^{-27}$ erg·s). The concentrations of RhB solutions were determined by UV-visible spectrophotometer (Jenway 7310, UK).

2.4 Photocatalysis experiments

The photocatalytic activity of the samples in terms of the photocatalytic decolorization of RhB aqueous solution was performed at ambient temperature. The visible-light source was provided by a 300 W Xe lamp (15 cm above the dishes) with a 400 nm cutoff filter as a light source. The UV-visible photocatalytic activity was evaluated using 300 W Xe lamp.

In the photocatalysis experiments, 0.008 g of the prepared photocatalyst powder was dispersed in a 40 mL RhB aqueous solution with a concentration of 10 mg/L in a beaker. The mixed solution was remained in dark for an hour to establish the RhB solution adsorption-desorption equilibrium on the photocatalyst before light irradiation. During photocatalysis, 3 mL reaction solution was taken out in some irradiation interval and filtered to measure the concentration change of RhB using a UV-visible spectrophotometer (Jenway 7310, UK).

3. Results and discussion

3.1 TiO_2 nanocrystallites formation mechanism

The TiO_2 formation mechanism was illustrated in scheme 1. To our best knowledge, TDMAT is a very reactive organometallic compound sensitive to active hydrogen such as -OH, -COOH, -C=C-H to form gaseous $NH(CH_3)_2$. After treatment of CMK-3 with nitric acid, active functional groups (R-OH, R-COOH) and some C=C-H groups formed on the surface[26,32,33]. The active hydrogen on CMK-3 surface would react with the active Ti-N bonds, which lead to the formation of gaseous dimethylamine and R-O-Ti structure, as shown in scheme 1. The unreacted Ti-N bonds will be further hydrolyzed after the sample exposed to air under room temperature to generate the Ti-O bond. Since the hydrolysis and condensation of TDMAT occurred within the mesopores of CMK-3 during reflux process, the carbon restricted the growing up of the Ti-O-Ti structure. Following thermal treatment at 600 ℃ in argon atmosphere will lead to the improvement of Ti-O-Ti architecture unit and the carbon wall can still inhibit the grain growth of TiO_2 crystallites. More importantly, oxygen vacancies generated during the thermal treating in inert atmosphere due to the absence of oxygen[34]. Finally, the carbon template was completely removed by combustion in air.

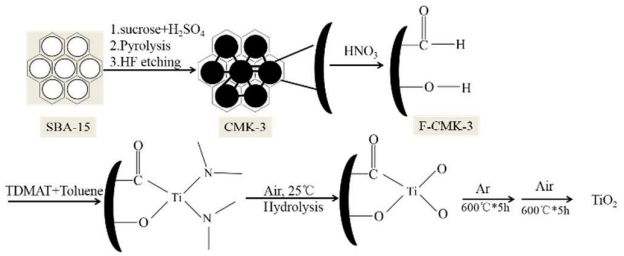

Scheme 1. The formation mechanism of nanocrystalline TiO_2 (black arc represents the wall of mesoporous carbon CMK-3, the Ti-O bond starts to form during refluxing process of TDMAT and tolunene, other unreacted Ti-N bonds break in air, thermal treatment can improve the Ti-O-Ti framework)

3.2 Characterizations of TiO_2

3.2.1 X-ray diffraction study

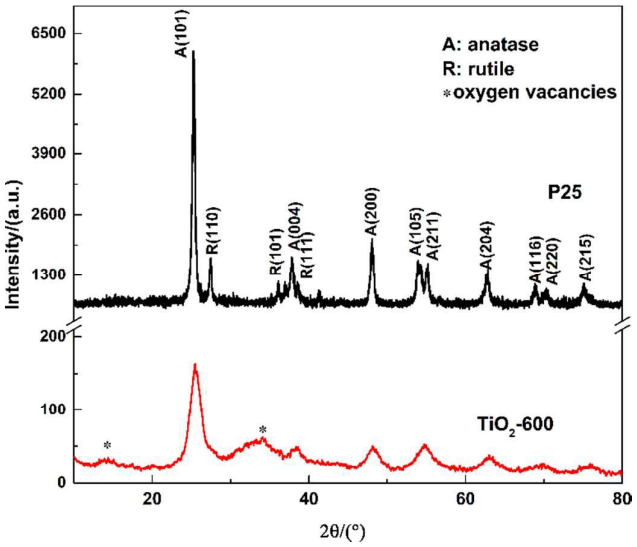

Fig. 1 X-ray diffraction patterns of TiO_2-600 and P25

The crystal structure of prepared samples was characterized by the wide-angle X-ray diffraction measurement. As shown in Fig. 1, the prepared TiO_2-600 and P25 exhibit totally different XRD patterns. P25 presents a mixed phase composition of 82.9% anatase and 17.1% rutile. For TiO_2-600, the reflection peaks at 25.3, 37.8, 48.04, 53.9, 55.1, 62.7, 68.8, 75.2 ° corresponded to the planes of (101), (004), (200), (105), (211), (204), (116), (220), (215), respectively, which can be well indexed to the tetragonal-anatase crystal phase (JCPDS NO. 84-1285)[14, 35-38], indicating that the prepared TiO_2-600 mainly consists of anatase crystal structure. Nevertheless, unassigned peaks can be observed at approximately 14.5 and 33.3 °, which are most likely attributed to TiO_{2-x}, and can be further proved to be oxygen defects by the XPS and EPR measurements, indicating that the oxygen

defects were produced during the annealing procedure. Before calcination in air, the CMK-3/TiO_2-600 exhibited typical anatase phase and mesoporous structure with shoulder peak in small angle XRD pattern (Fig. S4†), but the ordered mesoporous structures disappeared when removal of the carbon. Previous workers[14] have proved that the intensity of the reflection peaks is proportional to the crystallite size, so the obvious broadening of Bragg peaks of TiO_2-600 suggested the distinct decrease of crystallite size than P25. As listed in table 1, the crystallite size of prepared TiO_2-600 was calculated to be 5.0 nm according to the Scherrer formula ($a_0=K\lambda/\beta\cos\vartheta$, *K=0.9, λ=0.15405 nm*), which is much smaller than that of commercial P25. Meanwhile, the crystallite size is very similar to the pore diameter of CMK-3. Thus it is plausible that the titanium source was hydrolyzed and condensed within the definitely restrictive space of mesoporous CMK-3 to form nanocrystalline TiO_2 framework. The space-confinement effect of mesopores in hard template plays an important role in the obtaining of objective nanostructure.

Table 1 physical and chemical properties of TiO_2-600, CMK-3/TiO_2-600 and P25

samples	Crystallite size [a] (nm)	V_p (cm^3/g)	S_{BET} (m^2/g)	k_{RhB} [b] (min^{-1})	D_{pm} [c] (nm)
P25	50.1	0.18	51.2	0.012	3.15
CMK-3/TiO_2-600	8.6	0.49	759.3	—	3.44
TiO_2-600	5.0	0.74	228	0.058	2.18

[a] The crystallite size was calculated by Scherrer formula ($a_0=K\lambda/\beta\cos\vartheta$, K=0.9, λ=0.15405 nm), [b] The reaction kinetics constant derived from $-ln(c/c_0)$ *vs.* time, [c] the most probable pore size

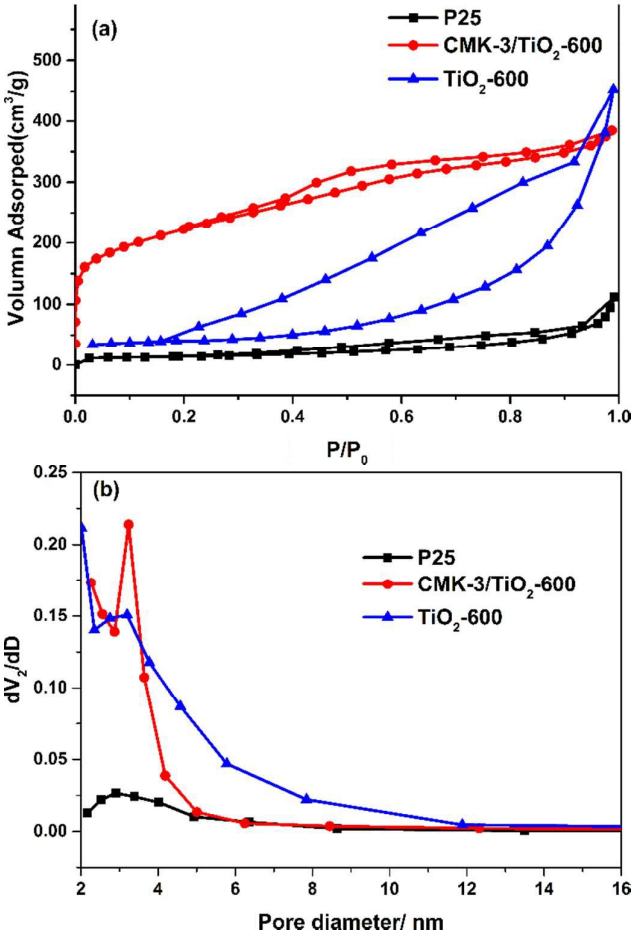

Fig. 2 The N_2 adsorption-desorption isotherms of P25, TiO2-600 and CMK-3/TiO_2-600 (a) and the corresponding pore sizes distribution curves (b)

N_2 adsorption–desorption isotherms and pore size distributions of P25, CMK-3/TiO_2-600 and TiO_2-600 are measured to analyze the porous properties of the as-synthesized samples. As shown in Fig. 2, the N_2 adsorption–desorption isotherms of TiO_2-600 belong to a typical type Ⅲ sorption behavior with a large type H3 hysteresis hoop, indicating the porosity of TiO_2-600. While CMK-3/TiO_2-600 appears to have a typical H4 hysteresis hoop, indicating the ordered mesoporous structure which mainly comes from the CMK-3. The lower adsorption of TiO_2-600 at relative pressure range (P/P_0=0.4-0.8) can also be observed, which may be attributed to the less number of mesopores compared to CMK-3/TiO_2-600. The results can be also confirmed by decreased tendency of the specific surface areas from 759.3 m^2/g of CMK-3/TiO_2-600 to 228 m^2/g of TiO_2-600[35]. Meanwhile, the most probable pore size of TiO_2-600 (Fig. 2b) is located at 2.18 nm and CMK-3/TiO_2-600 at 3.44 nm (shown in table 1). The results suggested that the nanocasting method using functioned CMK-3 and organic metal compounds was feasible to synthesize nanomaterials.

3.2.3 Raman scattering

Raman scattering, an effective supplement to XRD, is often used to analyze the microstructure change of nanocrystalline materials[2]. As for tetragonal anatase TiO_2 (symmetry group I41/amd-D19), composed of TiO_6 octahedra that share two adjacent edges in the ac- and bc-planes, six active modes ($3E_g$, $1A_{1g}$, $2B_{1g}$) in the Raman spectrum can be observed. However, the band at 517 cm^{-1} is resolved into two components at 507 cm^{-1} (A_{1g}) and 519 cm^{-1} (B_{1g}) only below 73 K[39]. Fig.3 presents the Raman spectra of TiO_2-600 and P25. The patterns display clearly Raman peaks in the range of 100–800 cm^{-1}. Five peaks can be observed in the spectra of TiO_2-600 and P25, the bands at 141 (E_g), 193 (E_g), 398 (B_{1g}) cm^{-1} correspond to the O-Ti-O bending vibration and the bands at 517 (A_{1g}, B_{1g}) and 638 cm^{-1}(E_g) to Ti-O stretching vibration, revealing the anatase TiO_2 has been successfully synthesized. From the Fig. 3, it is obvious that, the peaks of TiO_2-600 present apparent wideness and slight blue shift compared to that of P25, which is usually related to phonon confinement in small particles[10]. Meanwhile, it is acknowledged that the confinement would be present in individual particles rather than nanocrystallite derived from mesoporous structure[40]. However, in our case, the obtained TiO_2-600 possess nanocrystallite joined as mesoporous structure (Fig. 7). Furthermore, oxygen vacancies can also lead to a blue shift of the Raman peak, considering the sensitivity of E_g mode to the O-O interaction, we thus attribute the blue shift to the oxygen defects [40, 41, 42]. These defects are likely to share oxygen at the interfaces between TiO_2 nanocrystals [40]. The results indicate that our method promotes the formation of oxygen defects to some extent and have a remarkable impact on the Ti-O lattice, which is in accordance with that of XRD.

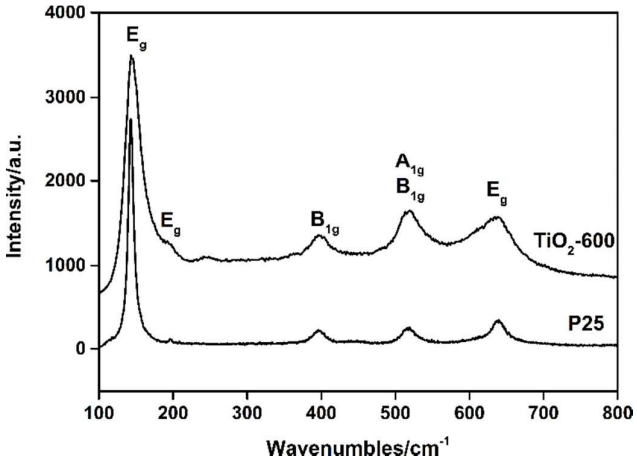

Fig.3 Raman sepctra of TiO_2-600 and P25

3.2.4 X-ray photoelectron spectroscopy study

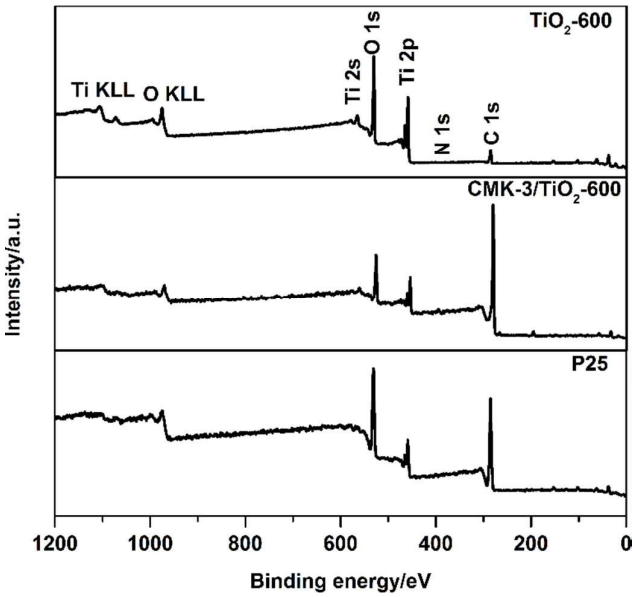

Fig.4 Wide survey XPS patterns ofTiO_2-600, CMK-3/TiO_2-600and P25

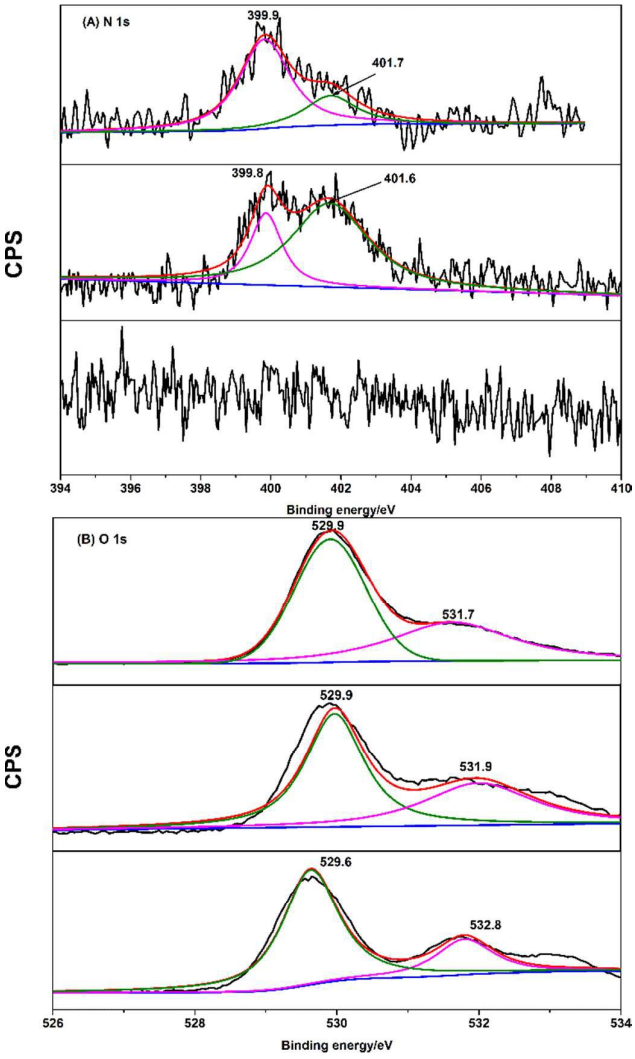

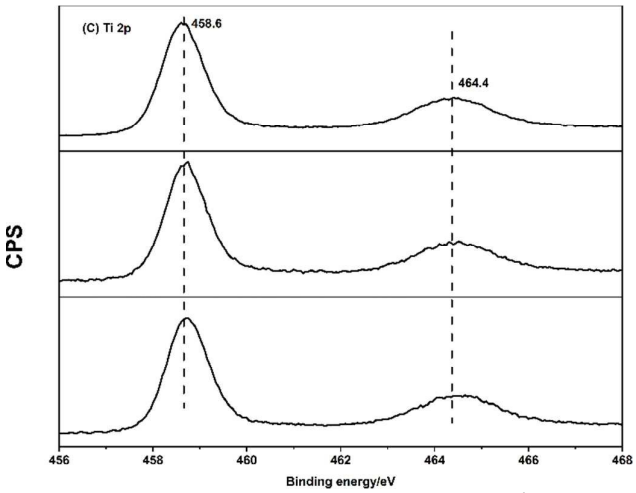

Fig.5 XPS spectra of TiO_2-600 (up), CMK-3/ TiO_2-600(middle) and P25 (below): (A) N 1s (B) O 1 s (C) Ti 2p XPS spectra

XPS spectra were acquired to analyze the surface chemical states and composition of CMK-3/TiO_2-600 and TiO_2-600. The wide survey XPS spectra (Fig. 4) indicate that the samples contains Ti, O, N and C. C element in TiO_2-600 may come from the adventitious C and the background[35]. TG results show that there are 82.55% and 1.37% of carbon left in CMK-3/TiO_2-600 and TiO_2-600, respectively (Fig. S4†) and the same tendency can be found from Fig. 4. The XPS spectrum of O 1s could be fitted by two peaks at binding energy of around 529.9 eV and 531.7 eV, which are principally attributed to the lattice oxygen of TiO_2 and the surface hydroxyl groups on titania, respectively[43]. From Fig. 5(b), we can observe much stronger intensity of CMK-3/TiO_2-600 at 531.7 eV, suggesting that there are much more hydroxyl groups in CMK-3/TiO_2-600. Meanwhile, the relatively weak intensity of TiO_2-600 indicates that thermal treatment can decrease the amount of surface hydroxyl groups. In comparison to P25 (529.6 eV), the O 1s spectrum of CMK-3/TiO_2-600 and TiO_2-600 slightly shifts to higher binding energy, which can be attributed to the oxygen vacancies. This is resulted from the decreasing of electro density of the O nearest to the oxygen vacancy for local deformation of TiO_2[44]. At the same time, the structure of the oxygen defect is more likely formed due to the relatively rapid removal of hydroxyl groups at 600 ℃ in argon atmosphere.

The core N 1s spectra of CMK-3/TiO_2-600, TiO_2-600 and P25 were depicted in Fig. 5(a). There's no N 1s peaks in P25, suggesting the absence of N elements. On the contrary, as for CMK-3/TiO_2-600 and TiO_2-600, the peak range from 396 to 404 eV corresponds to the typical peaks of N-doped TiO_2[1, 5, 14, 34], implying the N-doping in the TiO_2 lattice. In addition, there are two peaks at binding energy of around 399.9 eV and 401.8 eV. The peaks at 399.9 eV can be attributed to the interstitial nitrogen species or the oxidized nitrogen similar to NO_x species in the form as N-O-Ti or O- N-Ti accompany with the slight blue shift of Ti 2p spectra (Fig. 5c) according to previous work[14]. Herein, the intense peak at 399.9 eV by reason of anionic N in O-Ti-N has been reported[34]. N 1s core level peaks at 400–402 eV are ascribed to the adsorbed nitrogen on the surface of the catalyst in form of N-O-Ti[34]. The interstitial NO_x has a positive oxidation state leading to a higher binding energy shift. It is believed that N-doping would introduce impurity bandgap level upon the valence band, which would be donor level for electro generation under the visible light irradiation and hence improve the efficiency. What's more, the electron transfer within the O-Ti-O framework from oxygen vacancy to interstitial nitrogen species was effective for the bandgap narrowing of TiO_2[39]. Overall, N doping will not only facilitate the TiO_2 absorption spectrum moving to the visible light region but effectively improve the visible light photocatalytic efficiency. In our experiment, N-dopant may also come from the nitric acid during the pretreatment of CMK-3 since the samples have been put in air for a long time to promote the further reaction of residue $-N(CH_3)_2$ groups, as a result, TDMTA can completely react to form Ti-O-Ti structure.

The Ti 2p spectrum of TiO_2-600 was also observed (Fig. 5c) and the two peaks at around 464 and 458 eV, can be assigned to Ti $2p_{1/2}$ and Ti $2p_{3/2}$, respectively. Bousoulas [19] reported that titanium ions (Ti^{4+}) in oxygen vacancy enriched region might be reduced in order to fulfill the local charge neutrality. However, the absence of peaks at 457.5 and 463.1 eV confirms the absence of Ti^{3+} [24] and the anionic N can help to keep charge balance. And in general, N is considered to be a beneficial state for the photocatalytic performance[5, 45].Furthermore, the oxygen vacancies can be expected to create new bandgap levels[34]. Because no partial reduction of Ti^{4+} was found, the introduced levels would be closer to the conductive band edge[40]. Overall, the oxygen vacancies and N-dopants provide two additional bandgap levels which help to narrow the bandgap of pristine TiO_2 and enhance the photocatalytic activity under visible light irradiation. The surface O/Ti ratios from the XPS are greater than 2, which seemly contrary to that of XRD, but the excess oxygen on the surface may derive from the adventitious carbon or interstitial NO_x species.

3.2.5 Electron paramagnetic resonance study

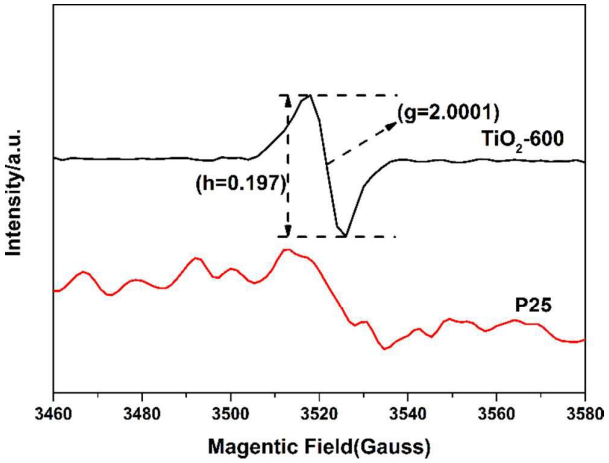

Fig.6 EPR spectra of the TiO_2-600 and P25

Electron paramagnetic resonance (EPR) is a most sensitive and accurate tool to detect the paramagnetic centers (N-

dapants or oxygen vacancies). Fig. 6 shows the different rhombic EPR signals of TiO_2-600 and P25. The characteristic g tensor is calculated to be 2.0010, which was very close to that of a standard free electro (g_e=2.0013), indicating the existence of single-electro-trapped oxygen vacancies (Vo·)[14, 42] induced by NO_x in the microenvironment either as Ti-NO_x-Vo· or the Ti-Vo··NO_x. The major EPR intensity of TiO_2-600 is higher than that of P25, means the relative concentration of Vo· is higher than pristine TiO_2. The relative higher Vo· concentration is associated with the thermal treatment in inert atmosphere. Additionally, the signal of Ti^{3+} can't be seen with g value at around 1.96, which is in accordance with the result of XPS.

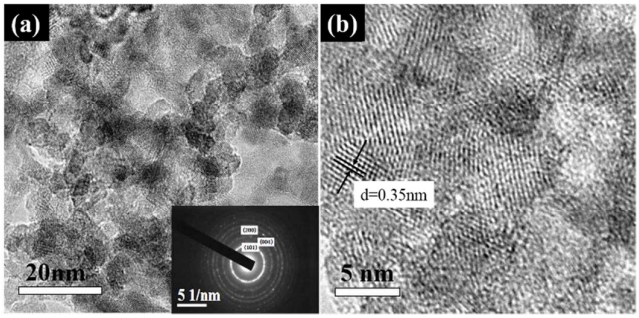

Fig. 7 TEM images of TiO_2-600 (a), the SAED image was inserted in (a); HRTEM image of TiO_2-600 (b)

3.2.5 The transmission electron microscope study

The microstructures of TiO_2-600 were observed via HRTEM as shown in Fig. 7. The images (Fig. 7a) clearly demonstrate the porous architecture of the sample. The sample is composed of highly crystalline particles with the size of 5 nm or so which is in good agreement with the result of XRD. The lattice fringes with d-spacing of 0.35 nm can be ascribed to the (101) planes of anatase TiO_2, revealing tetragonal crystal structure. The selected area electro diffraction patterns (inserted in Fig.7a) indicate that the sample is polycrystalline and confirms the formation of tetragonal phase by showing several diffraction rings corresponding to the TiO_2 (101) (004) (200) crystal plane, respectively. It is worth mentioning that, there are obvious lattice distortion on TiO_2-600 (Fig. 7b) with an enlargement of lattice spacing (d=0.61 nm), revealing the existence of large number of oxygen vacancies on the surface of TiO_2-600 which is in good agreement with XRD and Raman results.

3.3 Photocatalytic activity

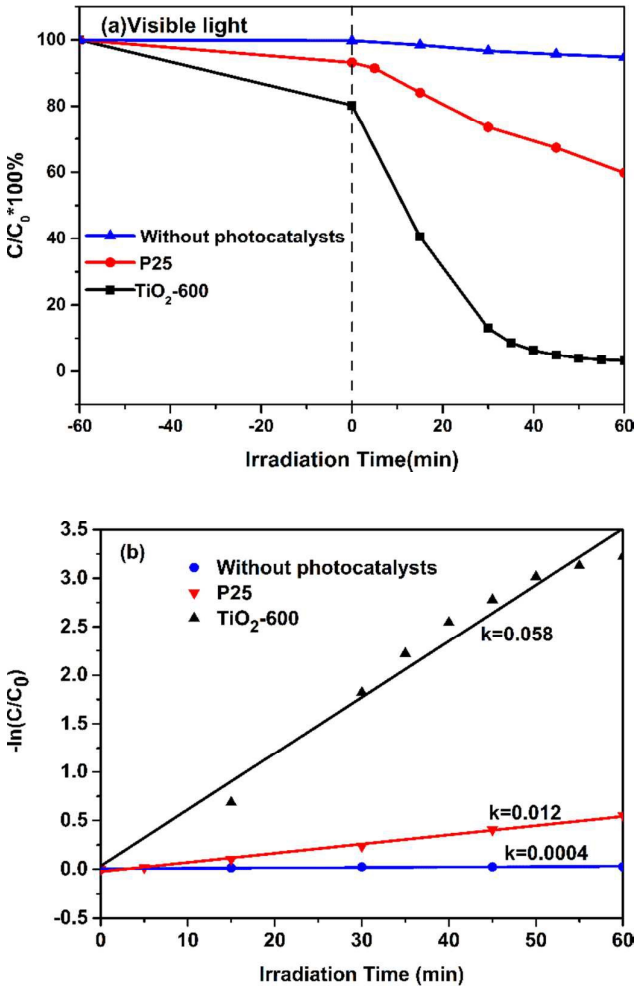

Fig. 8 Photocatalytic activity of TiO_2-600 and P25 under visible light irradiation (a) photocatalytic degradation of RhB (b) reaction kinetic ($ln(C/C_0)=-k_{app}t$) of visible-light photoreaction

The photocatalytic activity of TiO_2-600 was evaluated by photodegradation of RhB under the irradiation of visible light and UV-visible light. Fig. 8 demonstrates the photocatalytic activity and apparent reaction constant of TiO_2-600 under visible light irradiation. After being stirred for 60 min in dark, the adsorption capacities of TiO_2-600 and P25 were 19.7% and 6.8%, respectively. The degradation of RhB fits pseudo-first-order kinetics[34, 46], $-ln(C/C_0) = k\,t$, where the slope k is the apparent reaction rate constant, C is the concentration of RhB remaining in aqueous solution and C_0 is the initial concentration (10mg/L). Obviously, it can be found that TiO_2-600 have higher photocatalytic efficiency (96.5 %) than that of P25 (35.9 %) in 60 min. The broadening of excitation light to visible light range can be attributed to the sufficient oxygen vacancies and traces of N-dopants as proved by the previous characterization[47]. As shown in Fig. 8(b), the calculated apparent reaction rate constant of TiO_2-600 (0.058 min^{-1}) is 4.8 times of P25 (0.012 min^{-1}) (shown in table 1).

Fig. 9 shows the photocatalytic activity of TiO_2-600 and P25 under UV-visible light irradiation. As can be seen, the photolysis effect of RhB solution was very weak in 50 min, and TiO_2-600 showed relatively high activity under the UV-visible light irradiation, and a certain degradation efficiency of 96.8 % and 98.81 % was got after reaction in 50 min for P25 and TiO_2-600. The calculated apparent reaction rate constant of TiO_2-600 (0.084 min^{-1}) is 1.35 times of P25 (0.062 min^{-1}) (Fig. 9b).

In conclusion, TiO_2-600 sample exhibits higher photocatalytic efficiency than P25 under visible as well as UV visible light. The improved photocatalytic activity for TiO_2-600 is most likely dependent on the superior properties in terms of crystallite size, oxygen vacancies, specific surface areas[16, 46, 48], etc. N-dopants and oxygen vacancy provided extra band levels, and help to narrow the band gap between the valence band and conduction band, which can improve photocatalytic properties of TiO_2-600 under visible light.

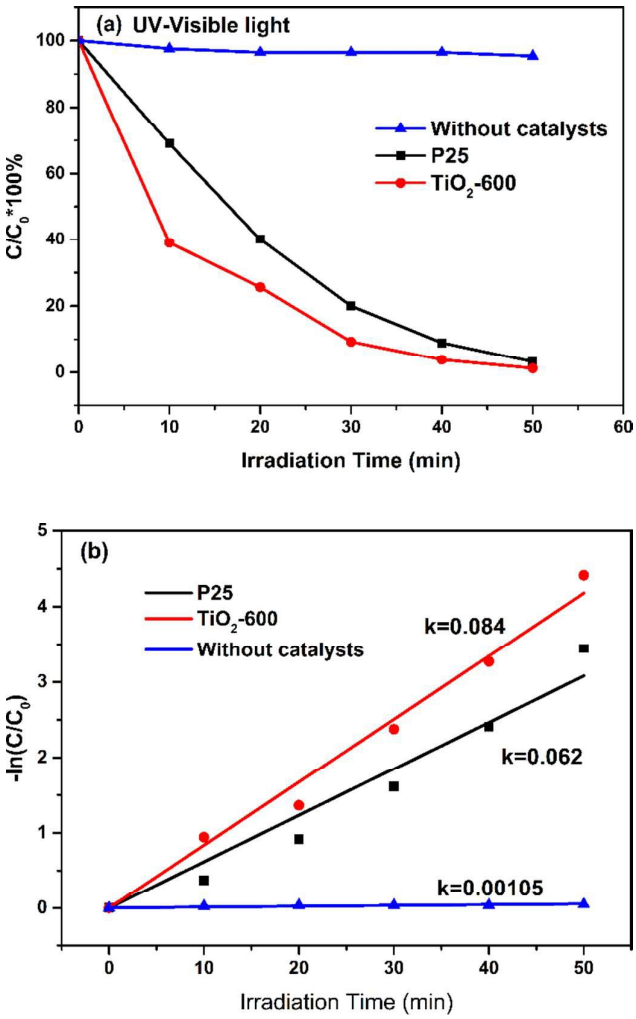

Fig. 9 Photocatalytic activity of TiO_2-600 and P25 under UV-visible light irradiation (a) photocatalytic degradation of RhB (b) reaction kinetic ($ln(C/C_0)=-k_{app}t$) of UV-visible light photoreaction

Conclusions

In summary, the nanocrystalline anatase TiO_2 with uniform size of 5.0 nm and sufficient oxygen vacancies is successfully prepared by a novel route in which mesoporous carbon (CMK-3) and organic metal composite (tetrakis (dimethylamino) titanium) have been used as hard template and titanium source. The introduction of active organometallic compounds (TDMAT) is confirmed that it can be bonded with the active hydrogen within the mesopores of CMK-3 and eventually form TiO_2 framework. Trace of N is introduced and doped into the lattice of TiO_2. The prepared sample exhibits high specific surface areas, sufficient oxygen vacancies, and enhanced photocatalytic activity for the degradation of RhB than P25 under the visible-light and UV-visible light irradiation. The synergistic effect between oxygen vacancies and N-dopants is responsible for the high visible-light activity. The research provides a methodology to synthesize nanocrystalline metal oxides by selecting special organometallic compounds and utilizing the space confinement effect of pores in molecular sieves.

Acknowledgements

We are thankful to Dr. Zheng Jiang and Dr. Lina Chi in University of Southampton for the photocatalytic experiments.

This work was financially supported by China-UK cooperation development and application of solar water splitting to hydrogen catalyst (2010081019).

Notes and references

1. S. Bouhadoun, C. Guillard, F. Dapozze, S. Singh, D. Amans, J. Boucle and N. Herlin-Boime, *Applied Catalysis B-Environmental*, 2015, **174**, 367-375.
2. F. Chen, Y. Li, Z. Liu and P. Fang, *Applied Surface Science*, 2015, **341**, 55-60.
3. W. Cheng, F. Rechberger, D. Primc and M. Niederberger, *Nanoscale*, 2015, **7**, 13898-13906.
4. P. R. Deshmukh, S. V. Patil, R. N. Bulakhe, S. N. Pusawale, J.-J. Shim and C. D. Lokhande, *Rsc Advances*, 2015, **5**, 68939-68946.
5. M. A. Mohamed, W. N. W. Salleh, J. Jaafar, A. F. Ismail and N. A. M. Nor, *Materials Chemistry and Physics*, 2015, **162**, 113-123.
6. 1, J. E. Mathis, J. J. Lieffers, C. Mitra, F. A. Reboredo, Z. Bi, C. A. Bridges, M. K. Kidder and M. P. Paranthaman, *Ceramics International*, 2016, **42**, 3556-3562.
7. J. Niu, S. Shen, S. He, Z. Liu, P. Feng, S. Zhang, X. Ou, Y. Qiang and Z. Zhu, *Ceramics International*, 2015, **41**, 11936-11944.
8. B. Chladkova, E. Evgenidou, L. Kvitek, A. Panacek, R. Zboril, P. Kovar and D. Lambropoulou, *Environmental Science and Pollution Research*, 2015, **22**, 16514-16524.
9. G. Cheng, F. Xu, F. J. Stadler and R. Chen, *Rsc Advances*, 2015, **5**, 64293-64298.
10. Z. Fan, F. Meng, M. Zhang, Z. Wu, Z. Sun and A. Li, *Applied Surface Science*, 2016, **360, Part A**, 298-305.
11. B.-R. Koo, H. An and H.-J. Ahn, *Ceramics International*, 2016, **42**, 1666-1671.
12. L. Yang, Q. Zhang, W. Wang, S. Ma, M. Zhang, J. Lv, G. He and Z. Sun, *Journal of Materials Science*, 2016, **51**, 950-957.

13. M. J. Sussman, A. Yasin and G. P. Demopoulos, *Journal of Power Sources*, 2014, **272**, 58-67.
14. Z. Jiang, L. Kong, F. Alenazey, Y. Qian, L. France, T. Xiao and P. P. Edwards, *Nanoscale*, 2013, **5**, 5396-5402.
15. J. Liu, S. Yu, W. Zhu and X. Yan, *Applied Catalysis a-General*, 2015, **500**, 30-39.
16. M. Amin, J. Tomko, J. J. Naddeo, R. Jimenez, D. M. Bubb, M. Steiner, J. Fitz-Gerald and S. M. O'Malley, *Applied Surface Science*, 2015, **348**, 30-37.
17. A. Kaur, A. Umar and S. K. Kansal, *Journal of Colloid and Interface Science*, 2015, **459**, 257-263.
18. Z. Li, Y. Zhu, F. Pang, H. Liu, X. Gao, W. Ou, J. Liu, X. Wang, X. Cheng and Y. Zhang, *Ceramics International*, 2015, **41**, 10063-10069.
19. P. Bousoulas, J. Giannopoulos, K. Giannakopoulos, P. Dimitrakis and D. Tsoukalas, *Applied Surface Science*, 2015, **332**, 55-61.
20. P. Deak, B. Aradi and T. Frauenheim, *Physical Review B*, 2015, **92**.
21. Q.-q. Meng, J.-j. Wang, J. Huang and Q.-x. Li, *Chinese Journal of Chemical Physics*, 2015, **28**, 155-160.
22. L. Nguyen Hoang, N. Tien Quang, W. A. Dino and H. Kasai, *Surface Science*, 2015, **633**, 38-45.
23. S. Guo, J. Fan, Q. Xu and Y. Min, *Rsc Advances*, 2015, **5**, 64414-64420.
24. S. Ma, J. Xue, Y. Zhou, Z. Zhang, Z. Cai, D. Zhu and S. Liang, *Rsc Advances*, 2015, **5**, 64976-64982.
25. Y. Ren, Z. Ma and P. G. Bruce, *Chemical Society Reviews*, 2012, **41**, 4909-4927.
26. 1, W. Yue, X. Xu, J. T. S. Irvine, P. S. Attidekou, C. Liu, H. He, D. Zhao and W. Zhou, *Chemistry of Materials*, 2009, **21**, 2540-2546.
27. C. M. Ho, J. C. Yu, T. Kwong, A. C. Mak and S. Y. Lai, *Chemistry of Materials*, 2005, **17**, 4514-4522.
28. W. Li, Z. Wu, J. Wang, A. A. Elzatahry and D. Zhao, *Chemistry of Materials*, 2014, **26**, 287-298.
29. An-Hui Lu, Wolfgang Schmidt, Akira Taguchi, Bernd Spliethoff, Bernd Tesche and F. Sch¸th, *Angew.Chem.Int.Ed.*, 2002, **41**, 4.
30. D. Y. Zhao, J. L. Feng, Q. S. Huo, N. Melosh, G. H. Fredrickson, B. F. Chmelka and G. D. Stucky, *Science*, 1998, **279**, 548-552.
31. Shinae Jun, Sang Hoon Joo, Ryong Ryoo, Michal Kruk, Mietek Jaroniec, Zheng Liu, Tetsu Ohsuna and O. Terasaki, *J. Am. Chem. Soc.*, 2000, **122**, 2.
32. H. J. Amezquita-Garcia, J. R. Rangel-Mendez, F. J. Cervantes and E. Razo-Flores, *Chemical Engineering Journal*, 2016, **286**, 208-215.
33. I. U. Din, M. S. Shaharun, D. Subbarao and A. Naeem, *Ceramics International*, 2016, **42**, 966-970.
34. Y. Zhou, Y. Liu, P. Liu, W. Zhang, M. Xing and J. Zhang, *Applied Catalysis B-Environmental*, 2015, **170**, 66-73.
35. D. Lu, P. Fang, X. Liu, S. Zhai, C. Li, X. Zhao, J. Ding and R. Xiong, *Applied Catalysis B-Environmental*, 2015, **179**, 558-573.
36. J. W. Peterson, B. Gu and M. D. Seymour, *Science of the Total Environment*, 2015, **532**, 398-403.
37. K. Xu, Y. Guo, Q. Sun, S. Dong and Z. Li, *Research on Chemical Intermediates*, 2012, **39**, 1417-1428.
38. D. Zhang, H. Yin, Z. Li, Y. Zhou, T. Yu, J. Liu and Z. Zou, *Rsc Advances*, 2015, **5**, 65005-65009.
39. L. J. Hardwick, M. Holzapfel, P. Novák, L. Dupont and E. Baudrin, *Electrochimica Acta*, 2007, **52**, 5357-5367.
40. A. Moya, A. Cherevan, S. Marchesan, P. Gebhardt, M. Prato, D. Eder and J. J. Vilatela, *Applied Catalysis B-Environmental*, 2015, **179**, 574-582.
41. S. Kelly, F. H. Pollak and M. Tomkiewicz, *Journal of Physical Chemistry B*, 1997, **101**, 2730-2734.
42. A. Tarasov, A. Minnekhanov, G. Trusov, E. Konstantinova, A. Zyubin, T. Zyubina, A. Sadovnikov, Y. Dobrovolsky and E. Goodilin, *Journal of Physical Chemistry C*, 2015, **119**, 18663-18670.
43. L. Yu, X. Yang, J. He, Y. He and D. Wang, *Journal of Alloys and Compounds*, 2015, **637**, 308-314.
44. H. Li, Y. Guo and J. Robertson, *Journal of Physical Chemistry C*, 2015, **119**, 18160-18166.
45. M. Sahoo, A. K. Yadav, S. N. Jha, D. Bhattacharyya, T. Mathews, N. K. Sahoo, S. Dash and A. K. Tyagi, *Journal of Physical Chemistry C*, 2015, **119**, 17640-17647.
46. U. G. Akpan and B. H. Hameed, *Journal of Hazardous Materials*, 2009, **170**, 520-529.
47. S. Banerjee, D. D. Dionysiou and S. C. Pillai, *Applied Catalysis B-Environmental*, 2015, **176**, 396-428.
48. A. A. Ismail and D. W. Bahnemann, *Journal of Materials Chemistry*, 2011, **21**, 11686-11707.